Spot-shadowing optimization to mitigate damage growth in a high-energy-laser amplifier chain

Seung-Whan Bahk,[1,*] Jonathan D. Zuegel,[1] James R. Fienup,[2] C. Clay Widmayer,[3] and John Heebner[3]

[1]Laboratory for Laser Energetics, University of Rochester, 250 East River Road, Rochester, New York 14623, USA

[2]The Institute of Optics, University of Rochester, 275 Hutchison Road, Rochester, New York 14627, USA

[3]Lawrence Livermore National Laboratory, 7000 East Avenue, L-465, Livermore, California 94550, USA

*Corresponding author: sbah@lle.rochester.edu

Received 19 August 2008; accepted 28 October 2008;
posted 10 November 2008 (Doc. ID 100329); published 5 December 2008

A spot-shadowing technique to mitigate damage growth in a high-energy laser is studied. Its goal is to minimize the energy loss and undesirable hot spots in intermediate planes of the laser. A nonlinear optimization algorithm solves for the complex fields required to mitigate damage growth in the National Ignition Facility amplifier chain. The method is generally applicable to any large fusion laser. © 2008 Optical Society of America

OCIS codes: 140.3280, 220.1230.

1. Introduction

Large solid-state lasers, such as the National Ignition Facility (NIF) [1] and OMEGA EP [2], operate at high fluences to optimize energy extraction from the amplifiers, thus operating near the damage threshold of system optics, particularly near the output of the system, such as at the frequency-conversion crystals (FCCs) or gratings in the compressor unit of a chirped-pulse amplification system. As a result, there is always a risk of initiating laser damage that can grow with continued exposure until the optic must be replaced at great expense and interruption to laser operations. Damage growth can be significantly mitigated, or even halted, by reducing the beam fluence at the damage site [3,4]. Shadowing laser-induced damage initiation sites is an appealing approach. This can be accomplished by introducing a programmable mask or a static apodizer mounted on a translation stage at an image-relay plane earlier in the laser beam line. A general method for optimizing spot shadowing in large, solid-state lasers is useful since there are similarities among facilities, such as NIF, OMEGA [5], and OMEGA EP [2] in the United States, Laser Mega-Joule in France [6], GEKKO XII in Japan [7], and the Vulcan facility in the United Kingdom [8]. The back end of these lasers consists of booster (power) amplifiers, transport optics to the target area, FCCs or compressor gratings, and focusing optics [9]. The gratings in the compressor unit generally have a low damage threshold, so it is beneficial for gratings to have a damage site shadowed [10]. Using NIF as our model, the feasibility of spot shadowing is presented. The beam propagation effects of simple intensity-only shadowing using a full-system model is described first. A limit of this approach is identified and is overcome by extending the apodization profiles to include both amplitude and phase. Two approaches to identify suitable complex-valued profiles are demonstrated.

2. National Ignition Facility's Initial Simulation Results of Intensity-Only Flattop Spot Shadowing

The NIF front-end and beam line architecture is shown schematically in Fig. 1. A seed pulse from a master oscillator is injected into the preamplifier module (PAM), which conditions the temporal and

0003-6935/08/356586-08$15.00/0

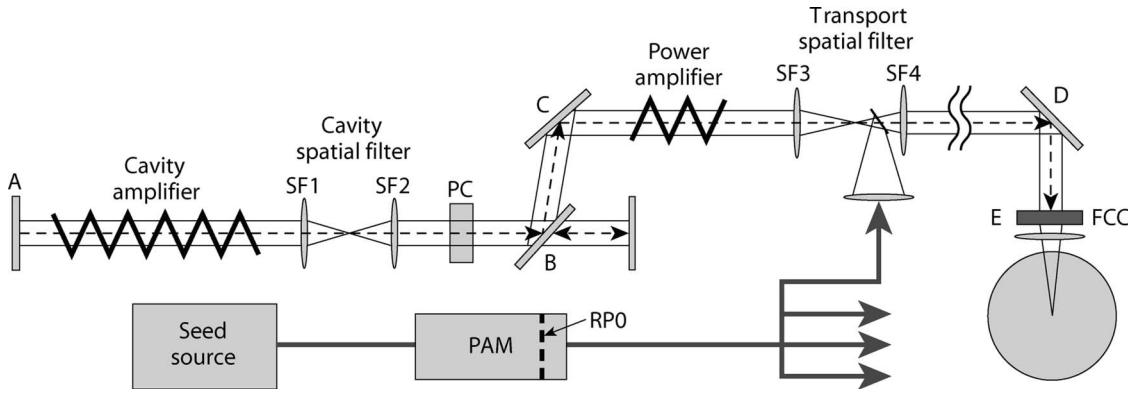

Fig. 1. Schematic of NIF front end and amplifiers. SF, spatial-filter lens; PC, Pockels cell; RP0, image-relay plane in the PAM; SF1 and SF2, cavity spatial filter; SF3 and SF4, transport spatial filter; A, C, and D, mirrors; B, polarizer. All focal lengths of SF3 and SF4 are 30 m. The distance from SF4 to FCC is approximately 62 to 74 m. depending on the location of each beam line. The half-acceptance angle of the transport spatial filter is 100 μrad on first pass (injection) and 200 μrad on second pass (last pass). Half-acceptance angle of the cavity spatial filter is 200 μrad for all four passes.

spatial profiles of a pulse and amplifies the pulse for injection into the main amplifier. The beam is split into four after the PAM and each sub-beam is injected into a main amplifier [11]. The main amplifier consists of a cavity amplifier and a power amplifier. After multiple passes through the cavity amplifier, the Pockels cell switches the beam to the power amplifier for a final energy boost. Beam propagation through each stage is controlled by an image-relaying spatial filter. After the last amplification stage, the pulse is image relayed to an FCC placed before the focusing optic. NIF, like any other laser fusion facility, is equipped with a large number of costly FCCs in the final focus-region optics. These must be protected from hot-spot modulations, and it is desirable to mitigate any damage growth on them. One possibility is to cast a spot shadow in the beam upstream, hoping that the exact spot shadow is imaged to the FCC unit. Detailed NIF laser simulations using the "PROP" [12] code indicate that satisfactory shadowing can be achieved in the FCC plane for a range of spot-size diameters (0.5 to 2 cm), where smaller shadow spots that obscure less of the beam are preferable. Lineouts of the calculated beam

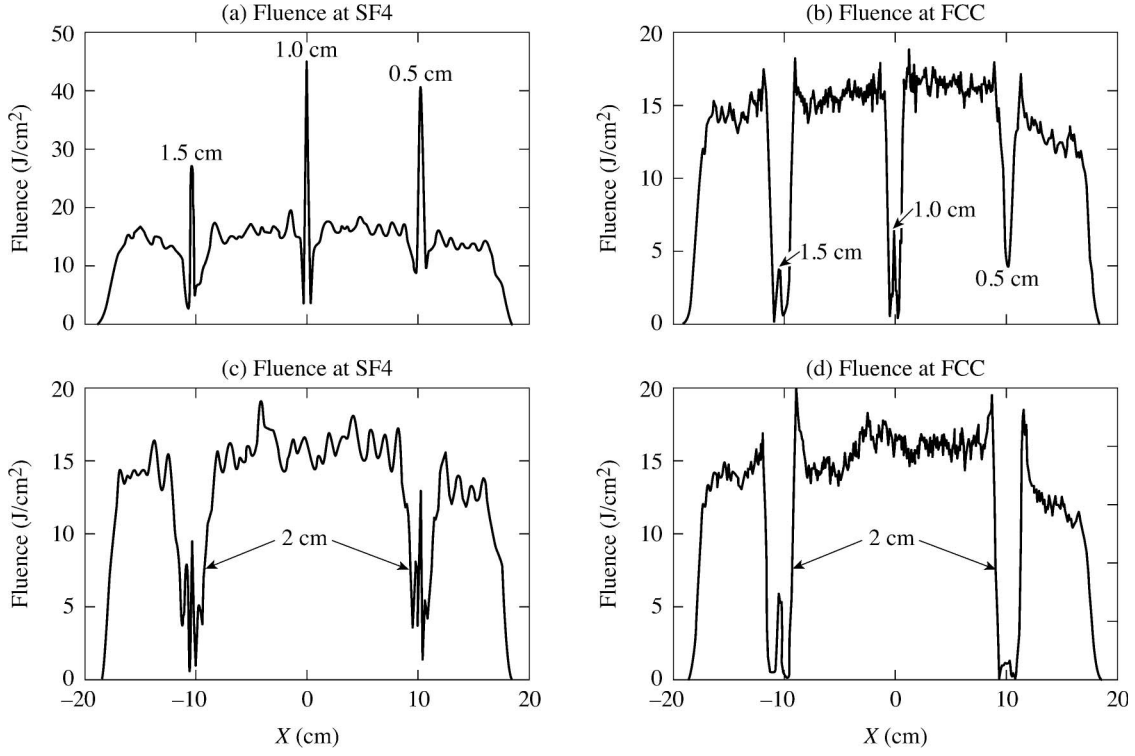

Fig. 2. Summary of initial NIF intensity-only spot-shadowing results. Beam line out at (a) SF4 and at (b) FCC using 0.5, 1, and 1.5 cm diameter flattop profile holes. Beam line out at (c) SF4 and at (d) FCC using 2 cm diameter flattop holes. The average fluence except at the holes is 16 J/cm^2, which corresponds to 3.4 GW/cm^2 using a 4.4 ns effective pulse width.

profiles at the transport spatial filter's output lens (SF4) and the FCCs are shown in Fig. 2 for locations centered behind different-size spot shadows introduced at the beam-shaping relay plane (RP0) in the PAM. This model uses a 4.4 ns FWHM Gaussian pulse as an alternative to the fully shaped ignition pulse (the Haan pulse). The Gaussian pulse introduces the same fluence and peak power as the Haan pulse. Unfortunately, excessive beam modulation as high as three times the normal beam fluence occurs at intermediate locations, such as the output lens of the transport spatial filter (SF4), when the spot shadows are smaller than 2 cm [Fig. 2(a)]. These hot spots are not classical Poisson spots, because the simulations show that they disappear by artificially setting the nonlinear index of optical material to zero or by reducing the intensity. This initial result may be acceptable if the energy loss due to a 2 cm obscuration spot is tolerable since the energy loss amounts to only 0.25% for a 40 cm × 40 cm beam. The cumulative effect of this energy loss, however, can be large, especially given the NIF architecture that multiplexes each front end to four beam lines. For example, if five FCC assemblies require spot shadowing, it may affect 20 out of 192 NIF beams. The energy loss will be 5% of total energy, equivalent to losing 10 beam lines. The residual peak in the spot shadow at the FCC plane, such as shown in Figs. 2(b) and 2(d) may have to be further reduced. It is important to investigate if a shadow profile at the output can be minimized in area by manipulating the phase as well as the amplitude of the spot.

3. Simplified System Modeling

The PROP code takes approximately 30 min to complete model propagation in a NIF beam line, so a simpler numerical model that retains all the essential features of the phenomenon was developed to implement an efficient iterative optimization. Simplification includes reducing the beam size and the number of data points, as well as the number of modeled physical processes that do not contribute to the main problem. The main physical processes included are free-space propagation, the optical Kerr effect, spatial filtering, and amplification. The physical effects not included in this model are gain inhomogeneity, aberrations, and high-spatial-frequency noise from optics. The multiple amplification steps in the multipass amplifiers are reduced to a single pass through the last pass of the multipass cavity and power amplifiers. This assumes that the nonlinear phase accumulation before the last pass in the cavity amplifier is negligible. The power density of the input beam to the last stage is taken from the PROP simulation. The input-beam distribution to the last pass is different from the field at RP0 (Fig. 1) only by the magnification in size and in amplitude and the modulation caused by spatial filtering in the intermediate planes. Although there are many spatial-filtering stages before injection into the main amplifiers, only the smallest pinhole size was applied once. In modeling the final amplification passes through the cavity and power amplifiers, each slab in the amplifiers is modeled with three lumped elements: amplification, nonlinearity, and free-space propagation to the next slab. There are 11 slabs in the cavity amplifier and 5 slabs in the power amplifier. The total propagation is from Planes A to E as shown in Fig. 1. The amplification was modeled after continuous wave (cw) amplification rather than by using the Frantz–Nodvik model [13] to avoid temporal integration. It is assumed that the peak intensity calculated from the full pulse amplification model at each step of amplification can alternatively be calculated by simply employing the cw model, where a proper choice of the saturation intensity is used. This

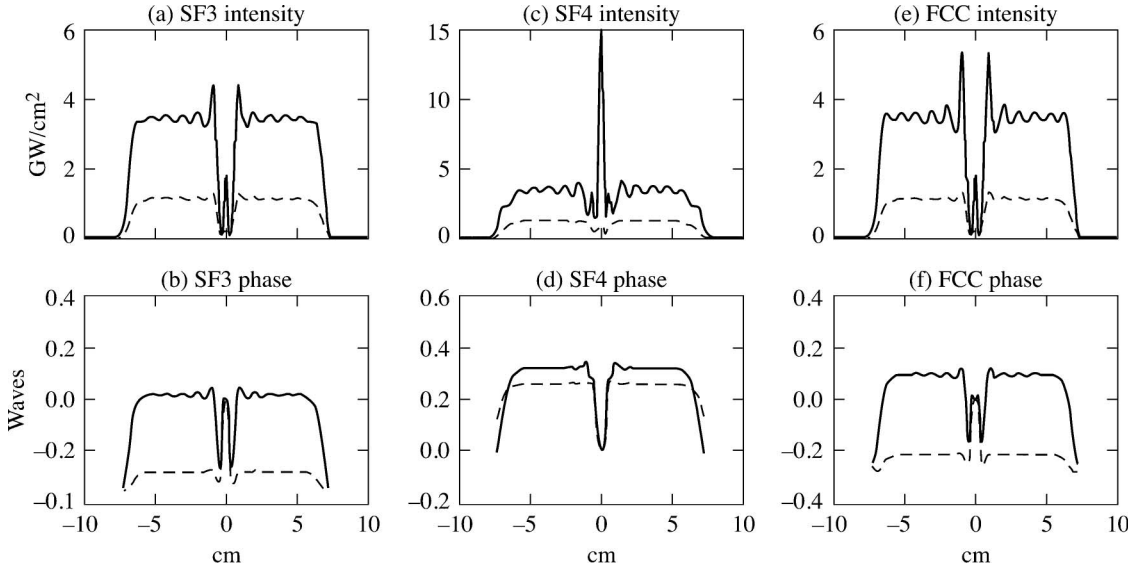

Fig. 3. Resimulation with a simplified code. Intensity and phase distributions at SF3, SF4, and FCC with increasing input power. Input energy of the solid curves is 10 times larger than that of the dotted curves. The input field is masked only in its amplitude with a flattop profile of a 1 cm diameter.

approach results in less than 3% discrepancy in the peak power compared with the full pulse amplification calculation for the last stage of amplification for a Gaussian pulse. The propagation through an image-relay telescope having a total length of $2F$ was modeled as Fresnel propagation of $-2F$ distance. Since an image relay usually incorporates spatial filtering, the total propagation effect through a spatially filtered telescope is achieved by filtering in the Fourier domain after the negative distance Fresnel propagation. Results from the simplified model confirm the same phenomenon predicted in full-system simulations by PROP. Figure 3 shows the calculated intensity and phase distributions at three different locations in the NIF laser system (SF3, SF4, and FCC) for low-energy (dashed red trace) and high-energy (solid blue trace) pulses for a mask at RP0 designed to produce a 1 cm diameter shadow spot at the FCC plane. The intensification at SF4 for the high-energy pulse is not present for lower intensities. The transport spatial filter's input lens (SF3) is approximately an image conjugate of the FCC plane, as expected from the geometry. Given this good agreement between the simplified and full models, we investigated if the system modeling can be further simplified using lumped elements. Simulations using a single step of amplification followed by a single step of nonlinear phase multiplication did not reproduce the hot spot observed in the spot shadow at SF4, so this level of simplification is not sufficiently accurate.

4. Nonlinear Self-Defocusing from a Spot-Shadow Profile and a Heuristic Solution

Ray tracing was used to identify which part of the laser beam at SF3 was most responsible for hot-spot formation at SF4 in the case of intensity-only shadowing of a 1 cm diameter spot. Given a phase map calculated from the simplified propagation method developed in Section 3, rays normal to the phase front can be assigned at each point in the beam. Tracing a uniformly distributed set of rays to the SF4 plane results in redistributed ray positions, where the concentration of rays represents the power density. The mapping of rays from an annular region with a 1 cm inner diameter and a 3 cm outer diameter is shown in Fig. 4. The initial radial position of rays at SF3 [Fig. 4(a)] is gray coded for tracking their redistribution at SF4 in Fig. 4(b). The central portion of SF3 [Fig. 4(a)] within the 1 cm diameter was not drawn, because the rays in this region diverge rapidly outside the spatial pinhole. It is graphically clear that the hot spot at SF4 originates from the region of nonzero intensity (black shade) just outside the central peak of the SF3 shadow spot. This region is marked with circles in Figs. 4(c) and 4(e). The energy from this region collapses to the axis behind the shadow spot at SF4, because the nonlinear wavefront defocuses this portion of the beam. For the 1 cm spot shadow, this defocus corresponds to a quadratic surface with an approximately 60 m radius of curvature. Combined with the 30 m focal length of spatial-filter lens SF3, the effective focal point is close to the location of SF4. Thus it is essential to control the curvature of this local defocusing region to prevent hot-spot formation. In the following paragraphs, we consider the possibility of modifying the local curvature using intensity-only shadowing and then a phase-only apodization option. It will be shown that both intensity and phase apodization are required to achieve a satisfactory result.

For intensity-only apodization, given an input phase profile that is constant across the beam, it is important to consider that the SF3 and FCC planes are nearly conjugate. Because of the image conjugacy, the requirement that a certain size of hole be formed at FCC results in a similar-size hole at SF3 plane. At high energies where nonlinearities dominate, the intensity pattern is directly imprinted onto phase by the optical Kerr effect; it can be seen that the size of the hole to be formed at the FCC determines the local defocusing curvature at SF3. For the case of a 1 cm diameter hole, it was shown that the collapse point is near the SF4 plane. Thus for the intensity-only approach to be successful in creating a hole less than 2 cm in diameter without forming a hot spot at SF4, the preceding analysis suggests that a hole diameter larger than 1 cm is required.

Next we consider a phase-only approach. A phase-only approach alone cannot achieve spot shadowing, because the RP0 plane is image relayed to the FCC by design. However, the phase response at the output for a given input phase profile is investigated. In a simple simulation, it was found that a low-order phase profile can, to some degree, be propagated through the system, preserving its shape. High-order phase is supposedly filtered out through the system's spatial filters. The resulting phase output is not exactly the same as the input phase profile due to the interplay between the nonlinear phase and intensity profile induced by phase modulation. The low-order phase profile chosen in the simulation is a fourth-order polynomial,

$$\phi(r) = 2\pi\eta \frac{r_2^2}{2\lambda F}\left[\left(\frac{r}{r_2}\right)^4 - \left(\frac{r}{r_2}\right)^2\right], \qquad r \le r_2, \tag{1}$$

where r_2 is an arbitrary outer radius covering the smaller effective spot radius, F is the effective focal length near r_2, and η is a scaling factor. This donut shape phase was chosen, because it can be naturally incorporated with the spot shadowing in the center. Figure 5 shows the effect of this low-order phase profile on the SF3 phase profile. It shows that the phase output at SF3 in the region outside the 1 cm diameter follows the direction and magnitude of the input phase, whereas the phase output within the 1 cm diameter region is not much affected by the sign of the input phase. Thus it suggests a controllability of the phase output at SF3 in the region outside the 1 cm diameter. This additional phase modulation can shift the width of the phase hole shown in Fig. 4(e) and

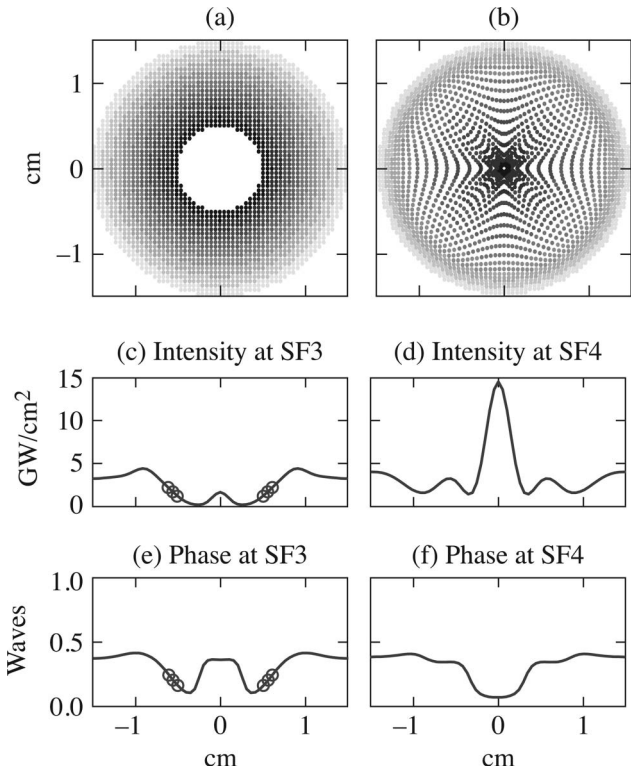

Fig. 4. Distribution of ray positions at SF3 and SF4 using 1 cm diameter spot shadowing. Each point represents a ray point and is gray coded for easy tracking. The black zone in (a) collapses to focus in (b), indicating that it is the main contributor to the SF4 hot spot. The black zone corresponds to the circled region of the shadow spot at SF3 intensity (c) and phase (e). Note that the rays in the hollow zone in (a) diverge outside the region of interest and were not drawn in this figure.

lengthen or shorten the radius of curvature following the sign of the low-order phase correction.

Based on these observations, we first attenuated the shoulder of the spot outside the 1 cm diameter hole to increase the nonlinear focal length as shown in Fig. 6(a). The intensity inside the 1 cm diameter is set to zero, whereas the intensity outside the 1 cm diameter and inside the 2 cm diameter is set to half of the nominal value. The nominal value is defined as the average intensity in the absence of a spot shadow. This stepwise intensity-only shadowing still induced a hot spot at the SF4 plane. Using the heuristic knowledge of the preceding phase response study, a fourth-order, positive phase was added to the stepwise intensity profile as shown in Fig. 6(b). The phase response at SF3 to the positive fourth-order phase input counteracts the phase response of intensity-only shadowing. As a result, the local curvature of the defocusing region at SF3, which previously caused a hot spot, is now flatter, as shown in Fig. 6(c), and the hot spot at SF4 disappears [Fig. 6(d)]. The spot shadow at the FCC plane is comparable, in the relative magnitude of the residual peak, to the result from the 2 cm intensity-only shadow shown in Fig. 2(d). On the other hand, the addition of the negative phase correction to the stepwise intensity apodization does not suppress the hot spot at SF4. The negative phase in principle enhances the size of phase hole at SF3 and consequently lengthens the nonlinear focal length, pulling the location of the hot spot inward. In detailed calculations, the size of phase hole at SF3 creates rather smooth curvature, and the local curvature at the 1 cm diameter remains close to 60 m in length; therefore using negative phase correction does not reduce hot-spot intensity at SF4.

5. Optimized Solution

The heuristic solution in the Section 4 guides us in obtaining a more optimized solution with the prescription that both intensity and phase profile need to be controlled, and the region of control must be outside the 1 cm diameter. With this in mind, we first define regions of interest as specified in Fig. 7. Region 1, denoted as Ω_1, is where the radius $(r) \le 0.5\,\mathrm{cm}$, Region 2 (Ω_2) is where $0.5\,\mathrm{cm} < r \le 1\,\mathrm{cm}$, and Region 3 ($\Omega_3$) is where $r > 1\,\mathrm{cm}$. We set amplitude values at zero in Region 1 and at nominal values in Region 3. It is Region 2 where radially symmetric field values will be optimized. A nonnegative error metric function based on arguments with field values in Region 2 is used to optimize important laser system performance at various planes that is given by

$$F(a_1, a_2, \ldots, \phi_1, \phi_2, \ldots) \equiv \alpha_1 F_1 + \alpha_2 F_2 + \alpha_3 F_3 + \alpha_4 F_4, \tag{2}$$

where F and F_i are error metrics, a_i and ϕ_i are the amplitude and phase values in Region 2 in the radial direction, and α_i is a weighting factor for the individual error metric. The first error metric (F_1) is expressed as

$$F_1 = |I_{\mathrm{SF4}}(r=0) - I_{\mathrm{SF4,nom}}|/I_{\mathrm{SF4,nom}}, \tag{3}$$

where $I_{\mathrm{SF4}}(r=0)$ is the intensity at the origin of the SF4 plane and $I_{\mathrm{SF4,nom}}$ is the nominal intensity at the SF4 plane. F_1 is used to minimize the hot-spot intensity at SF4. The next three error metrics (F_2, F_3, F_4) are defined at the FCC plane. F_2 and F_3 are used to minimize the residual peak intensity at the beam center and the power contained in the Region 1 at the FCC plane, respectively. They are expressed as

$$F_2 = I_{\mathrm{FCC}}(r=0)/I_{\mathrm{FCC,nom}}, \tag{4}$$

where $I_{\mathrm{FCC}}(r=0)$ is the intensity at the origin of the FCC plane, and $I_{\mathrm{FCC,nom}}$ is the nominal intensity at the FCC plane; and

$$F_3 = P_{\mathrm{FCC},\Omega_1}/P_{\mathrm{FCC},\Omega_1,\mathrm{nom}}, \tag{5}$$

where $P_{\mathrm{FCC},\Omega_1}$ is the power contained in Region 1, and $P_{\mathrm{FCC},\Omega_1,\mathrm{nom}}$ is the nominal power at the FCC plane. Finally the fourth error metric, F_4, is used to maximize the power in Region 2 at the FCC plane, the form of which is as follows:

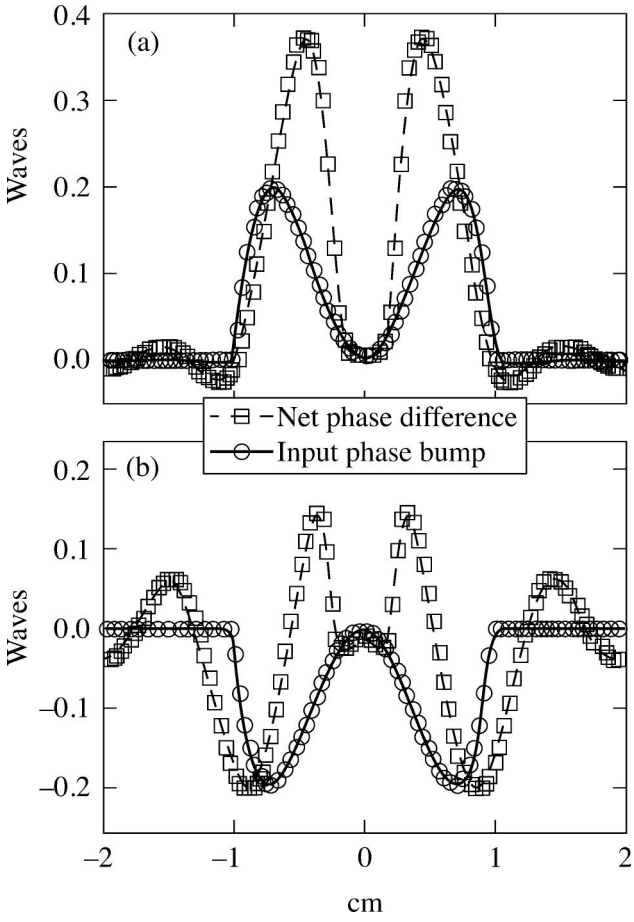

Fig. 5. Effect of low-order phase correction on the SF3-plane phase. Two cases of positive and negative low-order phase profiles are indicated by circles. The net phase difference is the difference in the SF3 phase with and without input phase correction. Input intensity was assumed uniform without any spot shadowing.

$$F_4 = |P_{\mathrm{FCC},\Omega_2,\mathrm{nom}} - P_{\mathrm{FCC},\Omega_2}|/P_{\mathrm{FCC},\Omega_2,\mathrm{nom}}. \qquad (6)$$

$P_{\mathrm{FCC},\Omega_2}$ is the power contained in Region 2, and $P_{\mathrm{FCC},\Omega 2,\mathrm{nom}}$ is the nominal power at the FCC plane, which is the same as $P_{\mathrm{FCC},\Omega_1,\mathrm{nom}}$.

Summarizing the meaning of each error metric, the first term (F_1) is the difference between the peak intensity at the origin and the nominal intensity level at SF4. The second term (F_2) is the peak intensity at the origin of FCC plane. The third (F_3) and fourth (F_4) terms are the power contained in Region 1 and the power loss in Region 2, respectively. Note that the reference value in F_1 error metric, i.e., $I_{\mathrm{SF4,nom}}$, does not need to be exactly this value, because one does not need to restrict the resulting value to be close to $I_{\mathrm{SF4,nom}}$. Once the form of the error metric is given, a solution is obtained by using a nonlinear conjugate gradient algorithm, which is based on a Polak–Ribiere version [14]. The initial values for the amplitude at RP0 are set to the nominal values, and the phase values are all set to zero. The search gradient is numerically calculated at each step. Figure 8 shows the progress of the each component of the error metric as the iteration number increases using weighting factors of 4, 1, 1, 0.5 that were established. It was empirically found that the first weighting factor for the hot spot at SF4 plane needs to be higher to sufficiently suppress it. It was also found that the fourth error metric for energy loss is more effective than the others, so the weighting factor for this component was decreased to balance with the others. It appears that the simultaneous minimization of the error metric 4 and 1 is difficult. The resulting optimum field distribution at RP0 and the intensity at SF4 and FCC planes are shown in Fig. 9. The optimization routine produces a solution that satisfies the requirements. The resulting phase distribution [Fig. 9(b)] is similar to the heuristic solution [Fig. 6(b)], whereas the optimized amplitude [Fig. 9(a)] results in 72% more energy in Region 2 at RP0 than in the heuristic solution shown in Fig. 6(a). The phase distribution at SF3, shown in Fig. 9(c), is similar to the heuristic result in Fig. 6(c). If one normalizes the energy outcome in Region 2 at the FCC plane from a 2 cm flattop hole to 1, the heuristic approach produces 13 more energy output in Region 2 and the optimization 14 more output. Although the improvement achieved by the optimization is not significantly better than the heuristic results, it should not be taken as the inefficiency of the automatic search algorithm. The heuristic solution was provided here rather as an aid for adding physical meaning of the solutions; also, the heuristic approach may not be applicable in some cases.

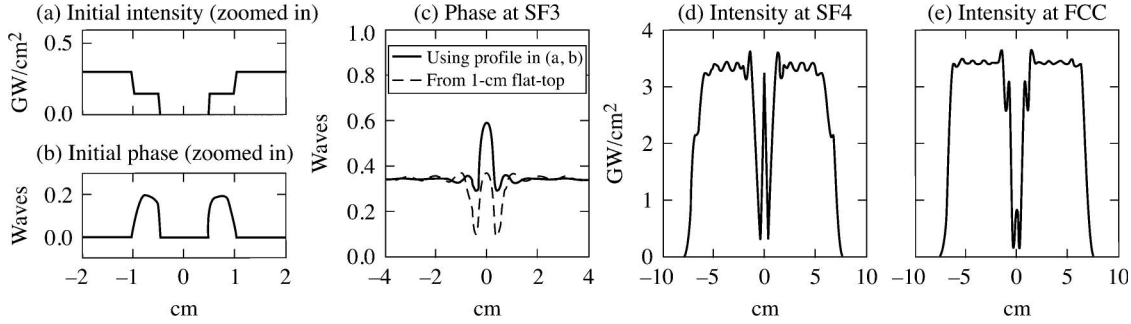

Fig. 6. Heuristic solution. (a), (b) Input intensity and phase at RP0, (c) phase at SF3, and (d), (e) intensity profile at SF4 and FCC planes, respectively.

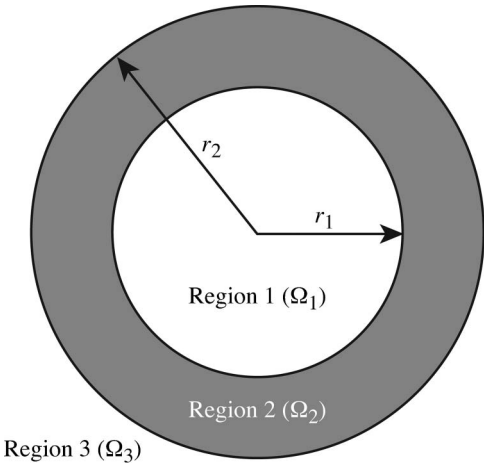

Fig. 7. Region denotations. r_1 is 0.5 cm, and r_2 is 1 cm. The origin is at the center of the beam. Radially symmetric intensity and phase distribution in Region 2 is optimized. Amplitude in Region 1 is always set to zero, and Region 3 denotes regular field distribution outside the spot shadow.

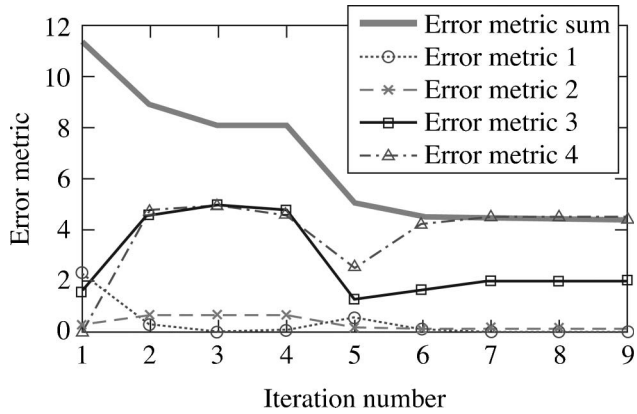

Fig. 8. The convergence of error metric components. Weighting factors for each component of the error metric are 4, 1, 1, 0.5. In the graph shown, weighting factors were not multiplied in the individual error metric component.

6. Conclusion

We have demonstrated a generalized technique for optimizing spot shadowing to mitigate damage growth near the back end of a high-energy laser system. Using NIF as the example, the possibility of reducing energy loss and residual bottom peak intensity at a critical location in the system has been presented by using an amplitude-phase-modulated spot of <2 cm diameter. For this effort, the cause of hot spots elsewhere in the laser system was identified as nonlinear self-defocusing from the shadow spot. A heuristic solution with the help of physical insight succeeds in compensating the nonlinear self-defocusing with a donut-phase correction term, while a systematic optimization technique employing a nonlinear conjugate gradient algorithm finds an optimal amplitude and phase-mask profile that meets all system requirements. The implementation of the complex-field, spot-shadowing scheme may be achieved by the application of a programmable spatial-light modulator. Bagnoud *et al.* [15] reported a single-plane, phase-only modulator that is able to control both amplitude and phase. The additional intensity manipulation capability in this scheme is made possible by encoding intensity information in a high-frequency phase carrier and filtering it through a spatial filter. The basic solutions, presented here, may be applicable to many other fusion lasers for spot shadowing. One other possible application of this approach can be shadowing of gaps in tiled-grating compressors. Many facilities around the world are adopting the tiling approach to provide the effective grating area needed to compress high-energy pulses [16,17]. The tiling gaps produce diffraction modulation downstream on the main transport and focusing optics that could cause damage. The gratings, for example, can intentionally be configured unsymmetrically so that a small amount of spatial chirp will smooth out the modulations from the gaps between tiles [18]. Spatial chirp induced in this way, however, may degrade pulse compression quality at the edge of the beam, and gap shadowing could be considered as an alternative.

This work was supported by the United States Department of Energy (DOE) Office of Inertial Confinement Fusion under Cooperative Agreement DE-FC52-08NA28302, the University of Rochester, and the New York State Energy Research and Development Authority. The support of DOE does not constitute an endorsement by DOE of the views expressed in this article.

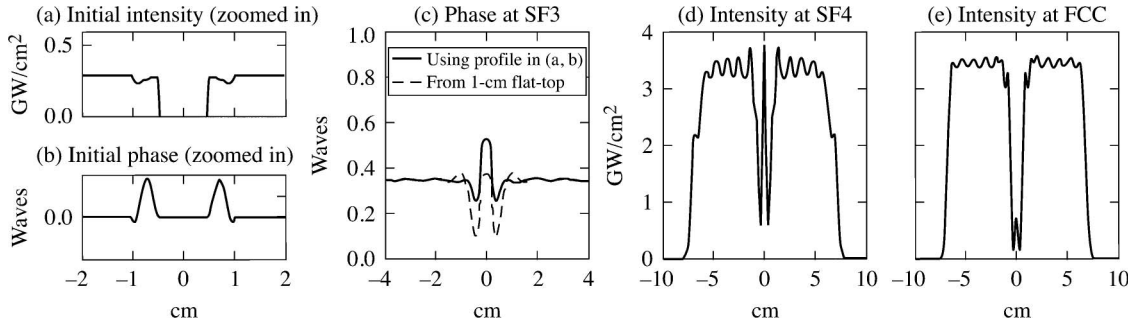

Fig. 9. Optimized solution. (a), (b) Input intensity and phase at RP0, (c) phase at SF3, and (d), (e) intensity profile at SF4 and FCC planes, respectively.

References

1. G. H. Miller, E. I. Moses, and C. R. Wuest, "The National Ignition Facility: enabling fusion ignition for the 21st century," Nucl. Fusion **44**, S228–S238 (2004).
2. J. H. Kelly, L. J. Waxer, V. Bagnoud, I. A. Begishev, J. Bromage, B. E. Kruschwitz, T. J. Kessler, S. J. Loucks, D. N. Maywar, R. L. McCrory, D. D. Meyerhofer, S. F. B. Morse, J. B. Oliver, A. L. Rigatti, A. W. Schmid, C. Stoeckl, S. Dalton, L. Folnsbee, M. J. Guardalben, R. Jungquist, J. Puth, M. J. Shoup, III, D. Weiner, and J. D. Zuegel, "OMEGA EP: High-energy petawatt capability for the OMEGA Laser Facility," J. Phys. IV **133**, 75–80 (2006).
3. M. A. Norton, E. E. Donohue, W. G. Hollingsworth, M. D. Feit, A. M. Rubenchik, and R. P. Hackel, "Growth of laser initiated damage in fused silica at 1053 nm," in *Laser-Induced Damage in Optical Materials: 2004*, G. J. Exarhos, A. H. Guenther, N. Kaiser, K. L. Lewis, M. J. Soileau, and C. J. Stolz, eds. (SPIE, 2005), Vol. 5647, pp. 197–205.
4. M. A. Norton, E. E. Donohue, W. G. Hollingsworth, M. D. Feit, A. M. Rubenchik, and R. P. Hackel, "Growth of laser initiated damage in fused silica at 1053 nm," Lawrence Livermore National Laboratory, Livermore, CA, Report UCRL-PROC-207885, NTIS Order No. DE2005-15014742 (2004).
5. T. R. Boehly, D. L. Brown, R. S. Craxton, R. L. Keck, J. P. Knauer, J. H. Kelly, T. J. Kessler, S. A. Kumpan, S. J. Loucks, S. A. Letzring, F. J. Marshall, R. L. McCrory, S. F. B. Morse, W. Seka, J. M. Soures, and C. P. Verdon, "Initial performance results of the OMEGA Laser System," Opt. Commun. **133**, 495–506 (1997).
6. A. Jolly, J. F. Gleyze, J. Luce, H. Coic, and G. Deschaseaux, "Front-end sources of the LIL-LMJ fusion lasers: progress report and prospects," Opt. Eng. **42**, 1427–1438 (2003).
7. Y. Kitagawa, H. Fujita, R. Kodama, H. Yoshida, S. Matsuo, T. Jitsuno, T. Kawasaki, H. Kitamura, T. Kanabe, S. Sakabe, K. Shigemori, N. Miyanaga, and Y. Izawa, "Prepulse-free petawatt laser for a fast ignitor," IEEE J. Quantum Electron. **40**, 281–293 (2004).
8. C. N. Danson, P. A. Brummitt, R. J. Clarke, J. L. Collier, B. Fell, A. J. Frackiewicz, S. Hancock, S. Hawkes, C. Hernandez-Gomez, P. Holligan, M. H. R. Hutchinson, A. Kidd, W. J. Lester, I. O. Musgrave, D. Neely, D. R. Neville, P. A. Norreys, D. A. Pepler, C. J. Reason, W. Shaikh, T. B. Winstone, R. W. W. Wyatt, and B. E. Wyborn, "Vulcan Petawatt—an ultra-high-intensity interaction facility," Nucl. Fusion **44**, S239–S246 (2004).
9. J. D. Zuegel, S. Borneis, C. Barty, B. LeGarrec, C. Danson, N. Miyanaga, P. K. Rambo, C. LeBlanc, T. J. Kessler, A. W. Schmid, L. J. Waxer, J. H. Kelly, B. Kruschwitz, R. Jungquist, E. Moses, J. Britten, I. Jovanovic, J. Dawson, and N. Blanchot, "Laser challenges for fast ignition," Fusion Sci. Technol. **49**, 453–482 (2006).
10. The damage mechanism on gratings may differ from regular optical surfaces; spot shadowing, however, can mitigate the damage growth on gratings whether they are metal or dielectric. Private communications with A. Schmid who specializes in measuring damage threshold at the Laboratory for Laser Energetics, University of Rochester.
11. R. H. Sawicki, "The National Ignition Facility: laser system, beam line design, and construction," in *Optical Engineering at the Lawrence Livermore National Laboratory II: The National Ignition Facility* (SPIE, 2004), Vol. 5341, p. 43.
12. W. H. Williams, J. M. Auerbach, M. A. Henesian, K. S. Jancaitis, K. R. Manes, N. C. Mehta, C. D. Orth, R. A. Sacks, M. J. Shaw, and C. C. Widmayer, "Optical propagation modeling for the National Ignition Facility," in *Optical Engineering at the Lawrence Livermore National Laboratory II: The National Ignition Facility*, M. A. Lane and C. R. Wuest, eds. (SPIE, 2004), Vol. 5341, pp. 66–72.
13. L. M. Frantz and J. S. Nodvik, "Theory of pulse propagation in a laser amplifier," J. Appl. Phys. **34**, 2346–2349 (1963).
14. W. T. Vetterling and B. P. Flannery, "Conjugate gradient methods in multidimensions," in *Numerical recipes in C: The Art of Scientific Computing*, 2nd ed., W. H. Press and S. A. Teukolsky, eds. (Cambridge University, 2002), Chap. 10, Sec. 6, p. 414.
15. V. Bagnoud and J. D. Zuegel, "Independent phase and amplitude control of a laser beam by use of a single-phase-only spatial light modulator," Opt. Lett. **29**, 295–297 (2004).
16. M. Hornung, R. Bödefeld, M. Siebold, M. Schnepp, J. Hein, R. Sauerbrey, and M. C. Kaluza, "Alignment of a tiled-grating compressor in a high-power chirped-pulse amplification laser system," Appl. Opt. **46**, 7432–7435 (2007).
17. J. Qiao, A. Kalb, M. J. Guardalben, G. King, D. Canning, and J. H. Kelly, "Large-aperture grating tiling by interferometry for Petawatt chirped-pulseamplification systems," Opt. Express **15**, 9562–9574 (2007).
18. H. Huang and T. J. Kessler, "Tiled-grating compressor configuration with uncompensated dispersion for reduction of near-field-intensity smoothing," Opt. Lett. **32**, 1854–1856 (2007).